# Insight-HXMT Observations of a Possible Fast Transition from the Jet- to Wind-dominated State during a Huge Flare of GRS 1915+105

L. D. Kong[1,2], S. Zhang[1], Y. P. Chen[1], S. N. Zhang[1,2], L. Ji[3], P. J. Wang[1,2], L. Tao[1], M. Y. Ge[1], C. Z. Liu[1], L. M. Song[1,2], F. J. Lu[1], J. L. Qu[1,2], T. P. Li[1,2,4], Y. P. Xu[1], X. L. Cao[1], Y. Chen[1], Q. C. Bu[1], C. Cai[1], Z. Chang[1], G. Chen[1], L. Chen[5], T. X. Chen[1], W. W. Cui[1], Y. Y. Du[1], G. H. Gao[1,2], H. Gao[1,2], M. Gao[1], Y. D. Gu[1], J. Guan[1], C. C. Guo[1,2], D. W. Han[1], Y. Huang[1], J. Huo[1], S. M. Jia[1], W. C. Jiang[1], J. Jin[1], B. Li[1], C. K. Li[1], G. Li[1], W. Li[1], X. Li[1], X. B. Li[1], X. F. Li[1], Z. W. Li[1], X. H. Liang[1], J. Y. Liao[1], B. S. Liu[4], H. W. Liu[1], H. X. Liu[1], X. J. Liu[1], X. F. Lu[1], Q. Luo[1,2], T. Luo[1], R. C. Ma[1], X. Ma[1], B. Meng[1], Y. Nang[1,2], J. Y. Nie[1], G. Ou[1], X. Q. Ren[1,2], N. Sai[1,2], X. Y. Song[1], L. Sun[1], Y. Tan[1], Y. L. Tuo[1,2], C. Wang[2,6], L. J. Wang[5], W. S. Wang[1], Y. S. Wang[1], X. Y. Wen[1], B. B. Wu[1], B. Y. Wu[1,2], M. Wu[1], G. C. Xiao[1,2], S. Xiao[1,2], S. L. Xiong[1], R. J. Yang[7], S. Yang[1], Y. J. Yang[1], Y. J. Yang[1], Q. B. Yi[1,2], Q. Q. Yin[1], Y. You[1], F. Zhang[1], H. M. Zhang[1], J. Zhang[1], P. Zhang[1], W. C. Zhang[1], W. Zhang[1,2], Y. F. Zhang[1], Y. H. Zhang[1,2], H. S. Zhao[1], X. F. Zhao[1,2], S. J. Zheng[1], Y. G. Zheng[1,7], and D. K. Zhou[1,2]

[1] Key Laboratory for Particle Astrophysics, Institute of High Energy Physics, Chinese Academy of Sciences, 19B Yuquan Road, Beijing 100049, People's Republic of China; kongld@ihep.ac.cn, szhang@ihep.ac.cn, chenyp@ihep.ac.cn
[2] University of Chinese Academy of Sciences, Chinese Academy of Sciences, Beijing 100049, People's Republic of China
[3] Institut für Astronomie und Astrophysik, Kepler Center for Astro and Particle Physics, Eberhard Karls, Universität, Sand 1, D-72076 Tübingen, Germany
[4] Department of Astronomy, Tsinghua University, Beijing 100084, People's Republic of China
[5] Department of Astronomy, Beijing Normal University, Beijing 100088, People's Republic of China
[6] Key Laboratory of Space Astronomy and Technology, National Astronomical Observatories, Chinese Academy of Sciences, Beijing 100012, People's Republic of China
[7] College of Physics Sciences & Technology, Hebei University, No. 180 Wusi Dong Road, Lian Chi District, Baoding City, Hebei Province 071002, People's Republic of China

## Abstract

We present the analysis of the brightest flare that was recorded in the Insight-HMXT data set in a broad energy range (2–200 keV) from the microquasar GRS 1915+105 during an unusual low-luminosity state. This flare was detected by Insight-HXMT among a series of flares during 2019 June 2 UTC 16:37:06–20:11:36 with a 2–200 keV luminosity of $3.4$–$7.27 \times 10^{38}$ erg s$^{-1}$. Basing on the broadband spectral analysis, we find that the flare spectrum shows different behaviors during bright and faint epochs. The spectrum of the flare can be fitted with a model dominated by a power-law component. Additional components show up in the bright epoch with a hard tail and in the faint epoch with an absorption line of $\sim 6.78$ keV. The reflection component of the latter is consistent with an inner disk radius $\sim$five times larger than that of the former. These results on the giant flare during the "unusual" low-luminosity state of GRS 1915+105 may suggest that the source experiences a possible fast transition from a jet-dominated state to a wind-dominated state. We speculate that the evolving accretion disk and the large-scale magnetic field may play important roles in this peculiar huge flare.

Unified Astronomy Thesaurus concepts: Black holes (162); X-ray binary stars (1811); Relativistic jets (1390); Accretion (14); Magnetic fields (994)

## 1. Introduction

The microquasar GRS 1915+105 is a black hole (BH) X-ray binary system characterized by abundant variabilities well distinguished from typical ones. It consists of a BH and a K-M III companion star (Greiner et al. 2001), which was first discovered by the GRANAT/WATCH all-sky monitor in 1992 (Castro-Tirado et al. 1992). The source was monitored thereafter by a series of telescopes like RXTE/ASM, Swift/BAT, MAXI/GSC, etc. and detected with complex temporal and spectral properties. Based on the light curves and color–color diagrams (CCDs), Belloni et al. (2000) and Klein-Wolt et al. (2002) classified the variations of its X-ray flux into at least 14 different classes. Some of these variability classes are believed to correlate with the limit cycles of accretion and ejection in an unstable disk; hence, the transitions between the A, B, and C states are defined in Belloni et al. (2000). The state connection between GRS 1915+105 and the canonical BH binary (Remillard & McClintock 2006) is not clear. Neilsen et al. (2011) presented the first detailed phase-resolved spectral analysis of the $\rho$ class ("heartbeat" oscillation),

which is characterized by regular oscillations with periods of 50–100 s, observed by Chandra and RXTE between the low-C state and the high-A/B states. They found that the jet is active at smaller scales during short X-ray hard states with 10% cycles near the minimum luminosity, and the disk wind at larger scales may lead the fast spectral transitions in different phases. From the "heartbeat" state, Zoghbi et al. (2016) also found two wind components with low velocities between 500 and 5000 km s$^{-1}$ and probably two more with high velocities reaching 20,000 km s$^{-1}$ ($\sim$0.06 c). Such an evolution of wind features may be associated with a bulge that is born in the inner disk and moves outward as the instability progresses (Zoghbi et al. 2016). Neilsen & Lee (2009) argued that the massive winds can affect the disk accretion flow and hence suppress or even quench jet formation, since the massive winds are preferentially but not exclusively detected in softer states where jet emission is generally absent or weak (Ponti et al. 2012; Homan et al. 2016). The less understood relations among the disk, jet, and wind as denoted by these results make GRS 1915+105 an appropriate laboratory for further explorations.

Until 2018 July, GRS 1915+105 remained bright. It entered an extended "unusually" low-flux state thereafter, characterized by a lower flux and harder spectrum (Koljonen & Tomsick 2020). Such a dramatic dimming has never been seen before and indicates that the source may be approaching its quiescent state. Different from other BH binaries, contemporary monitoring at the radio, IR, and X-ray bands detected strong variabilities in this "unusual" state of GRS 1915+105 (Koljonen et al. 2019; Murata et al. 2019; Trushkin et al. 2019a, 2019b, 2020; Vishal & Banerjee 2019). These variabilities at soft and hard X-rays were observed by MAXI/GSC, NICER, Swift/BAT, Astrosat, and Konus–Wind (Homan et al. 2019; Jithesh et al. 2019; Neilsen et al. 2019; Svinkin et al. 2019; Aoki et al. 2020; Takagi et al. 2020). A dust ring was detected on 2019 May 16 by Swift/XRT that could be the footprint of the strong flare that occurred a few days earlier (Iwakiri et al. 2019). Neilsen et al. (2019) found a bright flare from NICER observations on 2019 May 20 that lasted for 200 s and had a peak flux of 3400 counts s$^{-1}$. Their spectral analysis indicated that the flare has a hard continuum that is composed of a very strong and skewed iron line typical of relativistic reflection and a narrow line at ~6.4 keV. The average spectrum of the flare itself shows a deep iron absorption at ~6.65 keV. The Chandra gratings revealed a highly obscured state that may be relevant to the so-called "fail wind": a dense, massive accretion disk wind originates near the central engine but cannot escape because of low velocity (Miller et al. 2020).

The Hard X-ray Modulation Telescope, also dubbed Insight-HXMT, has been monitoring GRS 1915+105 and detected one flare with the longest duration and largest peak flux with respect to any other flares recorded in the Insight-HXMT data set during this new state. We analyze this huge flare in a broadband energy range (2–200 keV) covered by the three main detectors of Insight-HXMT: LE, ME, and HE. In this letter, we introduce the data reduction and analysis in Section 2 and present the results in Section 3. Finally, we offer discussion in Section 4 and conclusions in Section 5.

## 2. Observation and Data Reduction

Insight-HXMT (Zhang et al. 2014; Zhang et al. 2020) was launched on 2017 June 15 with a broad energy band (1–250 keV) and a large effective area in the high-energy range. Insight-HXMT consists of three collimated telescopes: the High Energy X-ray Telescope (HE, 18 cylindrical NaI(Tl)/CsI(Na) phoswich detectors; Liu et al. 2020), the Medium Energy X-ray Telescope (ME, 1728 Si-PIN detectors; Cao et al. 2020), and the Low Energy X-ray Telescope (LE, swept charge device; Chen et al. 2020). They have collecting areas/energy ranges of ~5100 cm$^2$/20–250 keV, ~952 cm$^2$/5–30 keV, and ~384 cm$^2$/1–10 keV and typical fields of view of 1°.6 × 6°, 1° × 4°, and 1°.1 × 5°.7; 5°.7 × 5°.7 for LE, ME, and HE, respectively.

Insight-HXMT has observed the microquasar GRS 1915+105 since 2017 June 15 (MJD 57,919), which sums up to 115 observations and a total exposure of ~2250 ks. Insight-HXMT detected a huge flare during 2019 June 2 UTC 16:37:06–20:11:36 (MJD 58,636.69−58,636.84) that lasted for about 13 ks. We focus on this flare and perform the analyses with Insight-HXMT Data Analysis Software (HXMTDAS) v2.02 (http://hxmt.org/software.jhtml). The data are selected under a series of criteria as recommended by the Insight-HXMT team: filter for the good time interval (GTI), elevation angle (ELV) larger than 10°, geometric cutoff rigidity (COR) larger than 8 GeV, offset for the point position smaller than 0°.04, and data removal with 300 s

more coverage of the South Atlantic Anomaly (SAA) passage. The energy bands are adopted for energy spectral analysis as 2–10 (LE), 10–35 (ME), and 27–200 (HE) keV, considering the background level and exposure. The backgrounds are estimated with the official tools, LEBKGMAP, MEBKGMAP, and HEBKGMAP in version 2.0.9, based on the standard Insight-HXMT background models (Guo et al. 2020; Liao et al. 2020a; Liao et al. 2020b). The XSPEC v12.10.1f software package (Arnaud 1996) is used to perform the spectral fitting. The uncertainty estimated for each spectral parameter is 90%, and a systematic error of 1% is added. The errors of the parameters are computed using a Markov Chain Monte Carlo (MCMC) of length 10,000.

## 3. Results and Discussion

### 3.1. The Flux and Color Evolution

The Insight-HXMT observations are shown in the left panel of Figure 1 (1 day time bin for each point), where an overall long-term evolution of GRS 1915+105 is obvious. The top three panels are the count rates of LE (1–10 keV), ME (10–20 keV), and HE (30–150 keV), respectively, and the bottom panel shows the hardness ratio of the ME/LE (soft color band) in a 1 day time bin. The source evolved to a low hard state at around MJD 58,300, with the hardness increasing from ~0.25 to 0.6. Its flux decreased after MJD 58,600 with a rapid increase of hardness ratio. Different from the quiescence of other BH binaries, there is a forest of X-ray and radio flares in this "unusual" low-luminosity state (Koljonen et al. 2019; Koljonen & Tomsick 2020; Murata et al. 2019; Trushkin et al. 2019a; Trushkin et al. 2019b; Trushkin et al. 2020). The brightest X-ray flare observed with Insight-HMXT occurred from 2019 June 2 UTC 16:37:06 (MJD 58,636.69) to 2019 June 2 UTC 20:11:36 (MJD 58,636.84). Following this event, a huge flare at radio band RATAN-600 appeared on 2019 June 3 at UTC 00:11 (Koljonen et al. 2019). The right panel of Figure 1 shows the details of this flare observed in ObsID P010131007501; the flare was decaying in snapshots of the first three (denoted as epochs 1–3) but almost ceased in the others (denoted as epochs 4–6). These monitorings suggest that the flare has a duration longer than 13 ks. Since the source had similar count rates in epochs 1 and 2 (~400 counts s-1 for LE and ME; ~1000 counts s-1 for HE), but dropped by half in epoch 3, our analyses are focused on the first three snapshots.

As for the investigations of the hardness–intensity diagram (HID) and CCD, we put this flare into the context of long-term evolution as observed by Insight-HXMT and find that the flare stands out significantly only in the HID (see the top two panels of Figure 2). The CCD and HID of the flare itself (see the bottom two panels of Figure 2) show that epochs 1 and 2 are located in a region significantly different from epoch 3 and epochs 4–6. This indicates that the source may experience a spectral transition during this peculiar short flaring period.

### 3.2. The Spectral Analyses

The spectral analyses are focused on epochs 1–3 (see Table 1 and Figure 3), and comparisons are made with respect to epochs 4–6 (see Figure 4). For GRS 1915+105, the mass of the BH, distance to the source, and inclination angle of the disk are taken as 12.4 $M_\odot$, 8.6 kpc, and 60° in estimating the inner radius and luminosity (Reid et al. 2014). The spectral analysis is carried out in a broad energy range (2–200 keV), which covers 2–10 keV
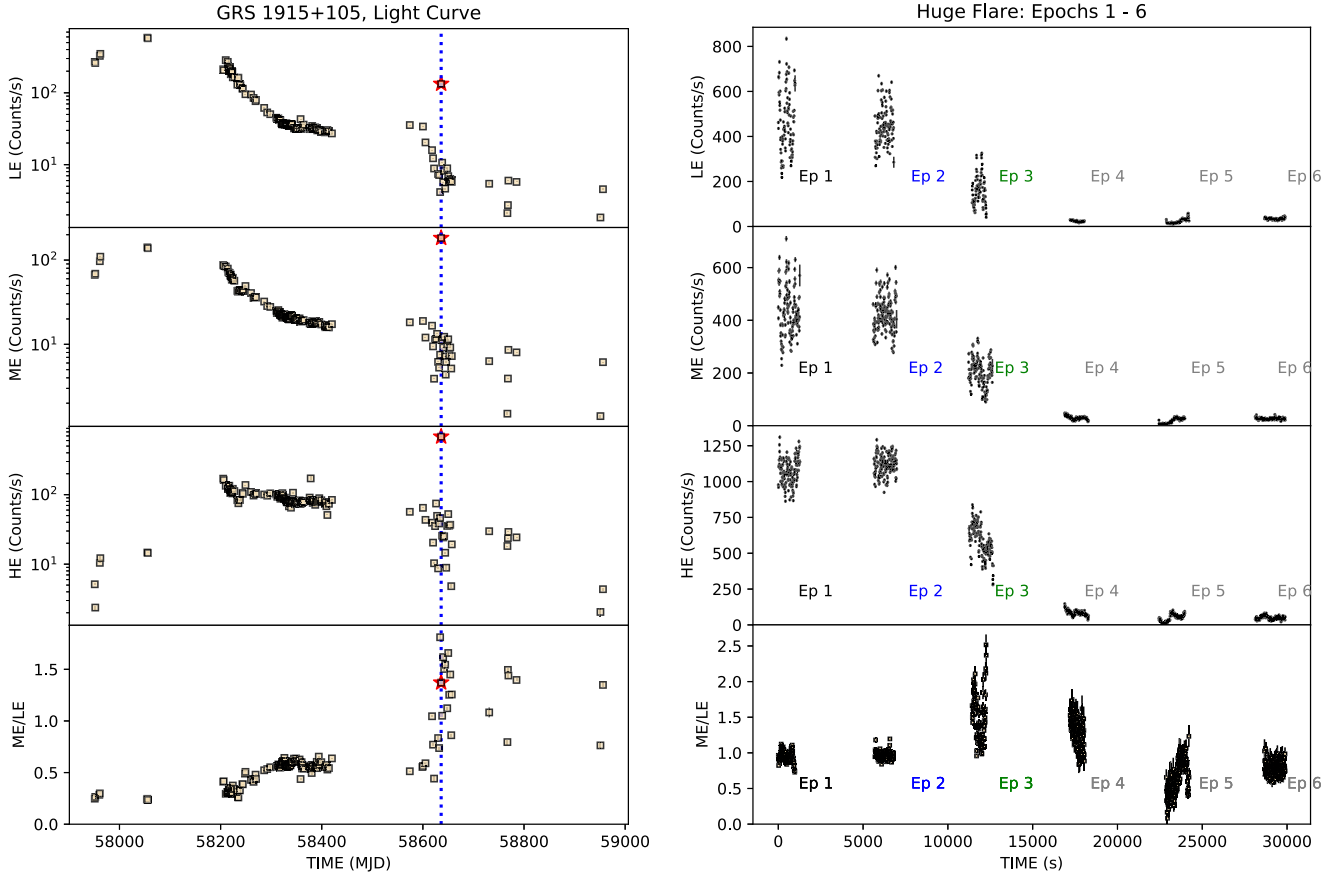
**Figure 1.** In the left panel, the light curves show observations in the broadband energy range by LE (1–10 keV; first plot), ME (10–20 keV; second plot), and HE (30–150 keV; third plot) with Insight-HXMT from 2017 July 11 to 2020 April 17. The hardness ratio of ME/LE is plotted in the bottom plot, and it shows a significant transition around the blue dotted line representing the position of the huge flare. The red star marks the huge flare. Right panel: detailed light curve and hardness ratio (10 s time bin) of the flare observed by Insight-HXMT from 2019 June 2 UTC 16:37:06 to 2019 June 2 UTC 20:11:36 (MJD 58,636.69 to 58,636.84). We separate the flare into three epochs.

for LE, 8–35 keV for ME, and 27–200 keV for HE. The first trial of fitting epochs 1–3 with $tbabs \times nthcomp$ results in residuals and $\chi^2_{red} > 2$ that are mostly attributed to an obvious asymmetry of the broadened iron line and a Compton hump between 10 and 30 keV. An absorption edge structure appears around 7.1 keV during epochs 1 and 2 but not epoch 3. The absorption edge was observed by both NICER and HXMT to accompany an emission line in the reflection component (Neilsen et al. 2020). Its origin still remains unclear, but we speculate that it may relate to the disk absorption of both the incident and reflected photons at the Fe K edge during the Compton scattering process. Accordingly, we use the $edge$ model to improve the fitting during epochs 1 and 2. Besides, an additional strong narrow absorption structure around 6.7–7 keV presents in epoch 3. Accordingly, the relativistic reflection model $relxill$ (García et al. 2014; Dauser et al. 2014) for three epochs and a Gaussian absorption line model $gabs$ in epoch 3 are introduced to improve the $\chi^2_{red}$. However, residuals still clearly exist above 50 keV for epochs 1 and 2 (see top and middle left panels in Figure 3), which required a power-law component. Finally, adoption of a model $tbabs \times edge \times (Gaussian+relxill+powerlaw)$ can fit the spectra with $\chi^2_{red} = 0.99$ and 0.96 for epochs 1 and 2, respectively. For epoch 3, one needs a modified model of $tbabs \times pcfabs \times gabs \times relxill$, which results in $\chi^2_{red} = 0.96$. The $pcfabs$ is used to account for additional absorption circumstances around the BH and avoid the sudden rising of the $n_H$ with $tbabs$ (Koljonen & Tomsick 2020).

Based on these spectral fittings, the luminosities (2–200 keV) are estimated for each epoch: $\sim 7.24$ and $7.27 \times 10^{38}$ erg s$^{-1}$ for epochs 1 and 2 and $\sim 3.4 \times 10^{38}$ erg s$^{-1}$ for epoch 3. The hydrogen column density $N_H$ is estimated with the Tuebingen–Boulder interstellar medium (ISM) absorption model $tbabs$ (Wilms et al. 2000) as $4$–$5 \times 10^{22}$ cm$^{-2}$ for the three epochs. As for epoch 3, the $pcfabs$ model gives an additional absorption of $\sim 11.8 \times 10^{22}$ cm$^{-2}$ from the matter with a covering fraction of $\sim 0.63$ during epoch 3.

For the $relxill$ components in the three epochs, the spin $a = 0.98$ and inclination angle $\theta = 60°$ are fixed during the spectral fittings (Reid et al. 2014). In the $relxill$ model, the reflect fraction $R_f$ is defined as the ratio of the incident photon intensity that illuminates the accretion disk to that observed directly, and $\gamma$ and $E_{cut}$ denote the initial spectral index and its deviation energy from a simple power-law shape. Other parameters in $relxill$ provide information about the accretion disk: the inner radius $R_{in}$, ionization of the accretion disk $\xi$, and iron abundance of the material $A_{Fe}$. During epochs 1 and 2, the reflection component can be adequately described by reprocessing of a hard spectrum with a low-energy cutoff ($\gamma \sim 1.02$, $E_{cut} \sim 22$–26 keV) in an accretion disk with an ionization of $\log \xi \sim 3.4$–3.6 and iron abundance $A_{Fe} \sim 3.58$–5 (in units of solar abundance). However, these parameters change significantly in epoch 3: lower $\log \xi \sim 1.4$ and $A_{Fe} \sim 0.61$, and a softer power-law spectrum with a spectral index of $\gamma \sim 2.42$ and higher cutoff energy
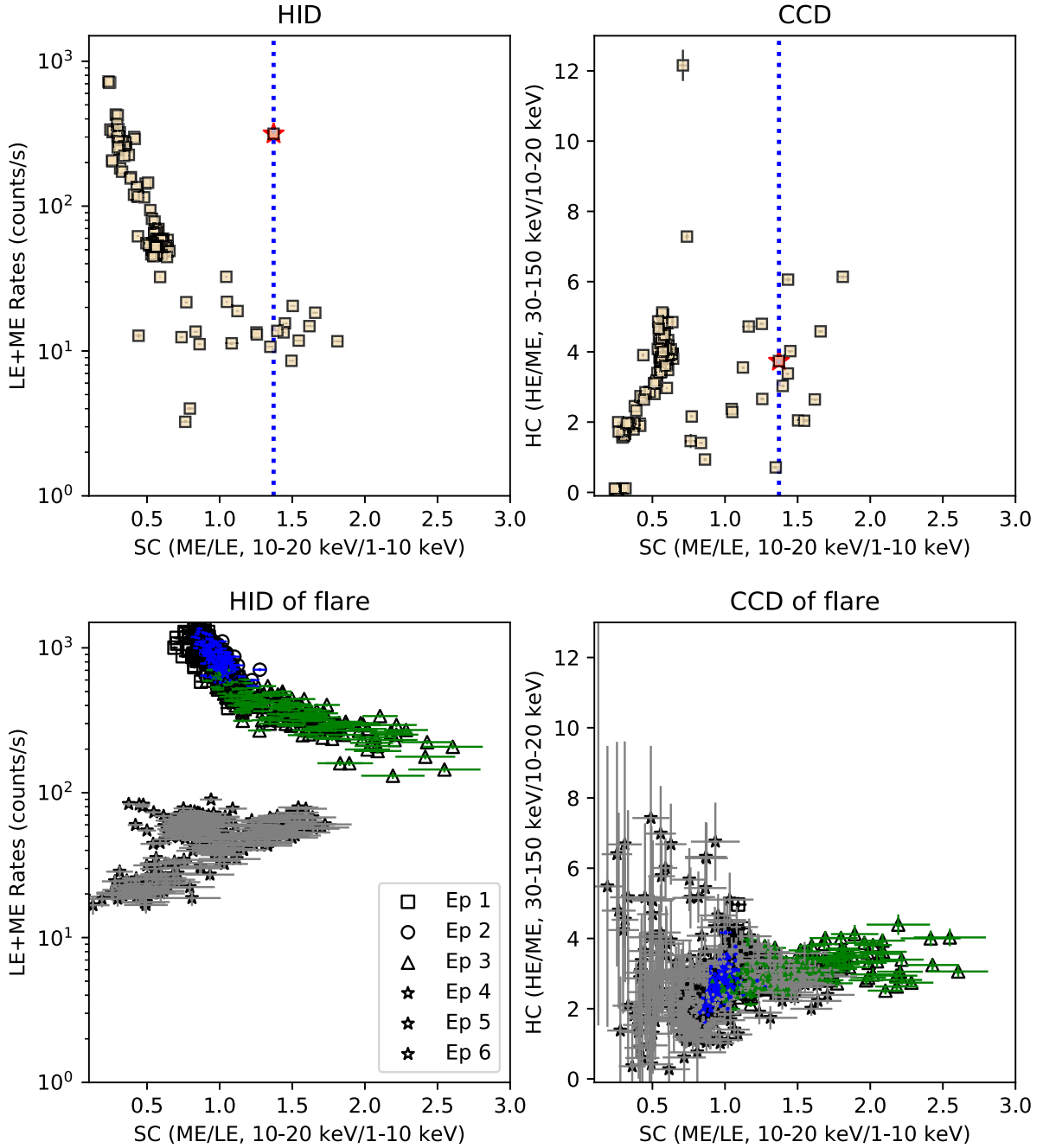
3

**Figure 2.** The CCD and HID of GRS 1915+105 with the same duration as Figure 1. The blue dotted line shows the position of the huge flare. The red star marks the huge flare. In the bottom panels, we separate the huge flare into six epochs, which are plotted in different colors as the same meaning as right panel in Figure 1.

$E_{\rm cut} \sim 195.95$ keV. The reflection fraction $R_{\rm f}$ increases from $\sim 0.28$–0.79 in epochs 1 and 2 to 2.71 in epoch 3.

An overall trend is that the inner disk tends to become larger through the three epochs; the inner radius is about 2 $R_{\rm ISCO}$ in epoch 1 and 5 $R_{\rm ISCO}$ in epoch 2 but increases to 13 $R_{\rm ISCO}$ in epoch 3. But the F-tests show no significant presence of a disk component in all three epochs. For epochs 1 and 2, we find that the residuals have some structures above 50 keV, which can be significantly accounted for by introducing a *powerlaw* component in the spectra (see the left panels in Figure 3). This component can extend to energies above 100 keV. The contributions of this component to the total luminosity are derived as $2.93^{+0.93}_{-0.85} \times 10^{37}$ erg s$^{-1}$ in epoch 1 ($\sim 3\sigma$) and $6.25^{+1.41}_{-1.46} \times 10^{37}$ erg s$^{-1}$ in epoch 2 ($\sim 4\sigma$). In epochs 1 and 2, narrow lines are found in

spectra with a centroid energy of $\sim 6.6$ keV and a line width of $\sigma \sim 100$–200 eV, probably associated with He-like Fe XXV emission. During epoch 3, accompanied by the absence of the power law and emission line and the appearance of an additional absorption line, we find a significant narrow absorption line at $6.78^{+0.02}_{-0.03}$ keV with a width of $\sigma = 143^{+26}_{-39}$ eV and a strength of $0.13^{+0.02}_{-0.01}$ ($\sim 9\sigma$; see bottom panels in Figure 3). Considering an energy resolution of 140 eV@5.9 keV for LE (Chen et al. 2020) and just a single absorption line detected by Insight-HXMT, the velocity of the outflow is hard to precisely estimate. Since the 6.78 keV absorption line may be relevant to the contamination of 6.98 keV, if any, which cannot be resolved by LE, we perform a spectral simulation by setting two absorption lines at 6.7 and 6.98 keV with the same line width of 0.14 keV but a different line

**Table 1**
Spectral Parameters of Three Epochs during the Flare

| Component | Parameters | Epoch 1 | Epoch 1 | Epoch 2 | Epoch 2 | Epoch 3 | Epoch 3 |
|---|---|---|---|---|---|---|---|
| *tbabs* | $n_{\rm H}$ ($10^{22}$ cm$^{-2}$) | $4.40^{+0.02}_{-0.06}$ | $4.51^{+0.04}_{-0.08}$ | $4.18^{+0.26}_{-0.25}$ | $4.45^{+0.02}_{-0.01}$ | $5.6^{+0.5}_{-0.9}$ | $5.53^{+0.69}_{-0.78}$ |
| *edge* | $E_{\rm edge}$ (keV) | 7.1 (fixed) | 7.1 (fixed) | 7.1 (fixed) | 7.1 (fixed) | ... | ... |
| | $\tau_{\rm Max}$ | $0.07^{+0.01}_{-0.02}$ | $0.03^{+0.01}_{-0.01}$ | $0.10^{+0.01}_{-0.01}$ | $0.10^{+0.01}_{-0.01}$ | ... | ... |
| *pcfabs* | $n_{\rm H}$ ($10^{22}$ cm$^{-2}$) | ... | ... | ... | ... | $11.8^{+2.4}_{-2.0}$ | $12.0^{+1.7}_{-1.3}$ |
| | $Cvr_{\rm F}$ | ... | ... | ... | ... | $0.63^{+0.10}_{-0.07}$ | $0.64^{+0.07}_{-0.08}$ |
| F-test | $F$-value | ... | ... | ... | ... | 34.6 | ... |
| | $P$-value | ... | ... | ... | ... | $2.14 \times 10^{-15}$ | ... |
| Gaussian | $E_{\rm line}$ (keV) | $6.60^{+0.05}_{-0.04}$ | $6.60^{+0.02}_{-0.01}$ | $6.57^{+0.03}_{-0.04}$ | $6.58^{+0.03}_{-0.03}$ | ... | ... |
| | $\sigma$ (eV) | $222^{+26}_{-11}$ | $238^{+38}_{-32}$ | $105^{+42}_{-33}$ | $132^{+15}_{-13}$ | ... | ... |
| | Norm ($10^{-2}$) | $2.2^{+0.5}_{-0.2}$ | $2.6^{+0.3}_{-0.2}$ | $1.0^{+0.2}_{-0.3}$ | $1.3^{+0.1}_{-0.1}$ | ... | ... |
| F-test | $F$-value | 32.6 | ... | 13.7 | ... | ... | ... |
| | $P$-value | $2.2 \times 10^{-20}$ | ... | $8.6 \times 10^{-9}$ | ... | ... | ... |
| *gabs* | $E_{\rm line}$ (keV) | ... | ... | ... | ... | $6.78^{+0.02}_{-0.03}$ | $6.75^{+0.01}_{-0.01}$ |
| | $\sigma$ (eV) | ... | ... | ... | ... | $143^{+26}_{-39}$ | $119^{+20}_{-30}$ |
| | Strength | ... | ... | ... | ... | $0.13^{+0.02}_{-0.01}$ | $0.13^{+0.01}_{-0.01}$ |
| *powerlaw* | $\Gamma$ | $1.78^{+0.03}_{-0.05}$ | $1.86^{+0.02}_{-0.06}$ | $1.98^{+0.02}_{-0.02}$ | $1.48^{+0.05}_{-0.05}$ | ... | ... |
| | Norm | $0.75^{+0.12}_{-0.22}$ | $1.07^{+0.12}_{-0.20}$ | $2.47^{+0.23}_{-0.30}$ | $0.16^{+0.04}_{-0.04}$ | ... | ... |
| F-test | $F$-value | 73.29 | ... | 71.63 | ... | ... | ... |
| | $P$-value | $4.2 \times 10^{-31}$ | ... | $1.93 \times 10^{-30}$ | ... | ... | ... |
| *relxill* | $R_{\rm in}$ ($R_{\rm ISCO}$) | $2.2^{+0.9}_{-0.3}$ | ... | $5^{+1}_{-1}$ | ... | $11^{+1}_{-3}$ | ... |
| | $\gamma$ | $1.04^{+0.02}_{-0.02}$ | ... | $1.00^{+0.02}_{-0.01}$ | ... | $2.42^{+0.04}_{-0.02}$ | ... |
| | $a$ | 0.98 (fixed) | ... | 0.98 (fixed) | ... | 0.98 (fixed) | ... |
| | $\theta$ | 60° (fixed) | ... | 60° (fixed) | ... | 60° (fixed) | ... |
| | $\log \xi$ | $3.60^{+0.11}_{-0.02}$ | ... | $3.44^{+0.02}_{-0.04}$ | ... | $1.40^{+0.03}_{-0.03}$ | ... |
| | $A_{\rm Fe}$ | $3.58^{+0.64}_{-0.17}$ | ... | $\leqslant 5.00$ | ... | $0.61^{+0.04}_{-0.05}$ | ... |
| | $E_{\rm cut}$ (keV) | $26^{+1}_{-1}$ | ... | $22.33^{+0.31}_{-0.23}$ | ... | $196^{+19}_{-12}$ | ... |
| | $R_{\rm f}$ | $0.79^{+0.09}_{-0.04}$ | ... | $0.28^{+0.03}_{-0.02}$ | ... | $2.71^{+0.38}_{-0.08}$ | ... |
| | $N_{\rm rel}$ ($10^{-2}$) | $3.70^{+0.25}_{-0.17}$ | ... | $5.93^{+0.32}_{-0.26}$ | ... | $8.31^{+0.56}_{-0.63}$ | ... |
| *relxilllp* | $h$ ($GM/c^2$) | ... | $5.56^{+0.52}_{-0.63}$ | ... | $6.78^{+0.27}_{-0.32}$ | ... | $30^{+4}_{-4}$ |
| | $R_{\rm in}$ ($R_{\rm ISCO}$) | ... | $1.34^{+0.04}_{-0.04}$ | ... | $1.14^{+0.03}_{-0.04}$ | ... | $5^{+3}_{-3}$ |
| | $\gamma$ | ... | $1.06^{+0.02}_{-0.02}$ | ... | $1.11^{+0.01}_{-0.01}$ | ... | $2.43^{+0.02}_{-0.05}$ |
| | $\log \xi$ | ... | $3.67^{+0.05}_{-0.03}$ | ... | $3.57^{+0.03}_{-0.03}$ | ... | $1.40^{+0.03}_{-0.03}$ |
| | $A_{\rm Fe}$ | ... | $3.33^{+0.15}_{-0.12}$ | ... | $3.26^{+0.15}_{-0.19}$ | ... | $0.60^{+0.05}_{-0.07}$ |
| | $E_{\rm cut}$ (keV) | ... | $23.59^{+0.76}_{-0.68}$ | ... | $25.70^{+0.26}_{-0.43}$ | ... | $196^{+15}_{-34}$ |
| | $R_{\rm f}$ | ... | $4.51^{+0.75}_{-0.47}$ | ... | $3.94^{+0.27}_{-0.29}$ | ... | $10.00^{+0.01}_{-0.01}$ |
| | $N_{\rm rel}$ ($10^{-2}$) | ... | $5.93^{+0.35}_{-0.92}$ | ... | $5.83^{+0.29}_{-0.27}$ | ... | $9.87^{+0.79}_{-0.61}$ |
| $L_{\rm PL}$ ($10^{37}$ erg s$^{-1}$) | 2–200 keV | $2.93^{+0.93}_{-0.85}$ | ... | $6^{+1}_{-1}$ | ... | ... | ... |
| $L_{\rm total}$ ($10^{38}$ erg s$^{-1}$) | 2–200 keV | $7.24^{+0.01}_{-0.03}$ | ... | $7.27^{+0.01}_{-0.03}$ | ... | $3.40^{+0.01}_{-0.02}$ | ... |
| Fitting | $\chi^2_{\rm red}/$dof | 0.99/1506 | 0.99/1505 | 0.96/1506 | 0.96/1505 | 0.96/1437 | 0.95/1436 |

**Note.** Uncertainties are reported at the 90% confidence interval and were computed using an MCMC of length 10,000. The 1% system error for LE, ME, and HE has been added during spectral fittings. The switch fixReflFrac in *relxilllp* is fixed at zero during the spectral fitting, allowing the reflection to fit freely.

depth of 2:1. The fitting result shows that an absorption line can exist at an energy similar to that observed in epoch 3. Actually, iron emission line of ∼6.6 keV is detected by combining the spectra of epochs 4–6 during the source flare almost ceased.

## 4. Discussion

We have carried out detailed analyses of a huge flare of GRS 1915+105 observed by Insight-HXMT during the low hard state of the source and obtained a few interesting results

during the decay phase in epochs 1–3 and ceasing phase in epochs 4–6.

The components of the power law and Fe emission line are present in epochs 1 and 2 but disappear in epoch 3, where instead an absorption line shows up at around 6.78 keV. The reflection component of the source spectrum suggests that the disk evolves outward, and the incident spectrum becomes softer and has a higher cutoff energy. Similar results can be derived by instead introducing a reflection model of *relxilllp* (see Table 1). Both the ionization of the accretion disk and the
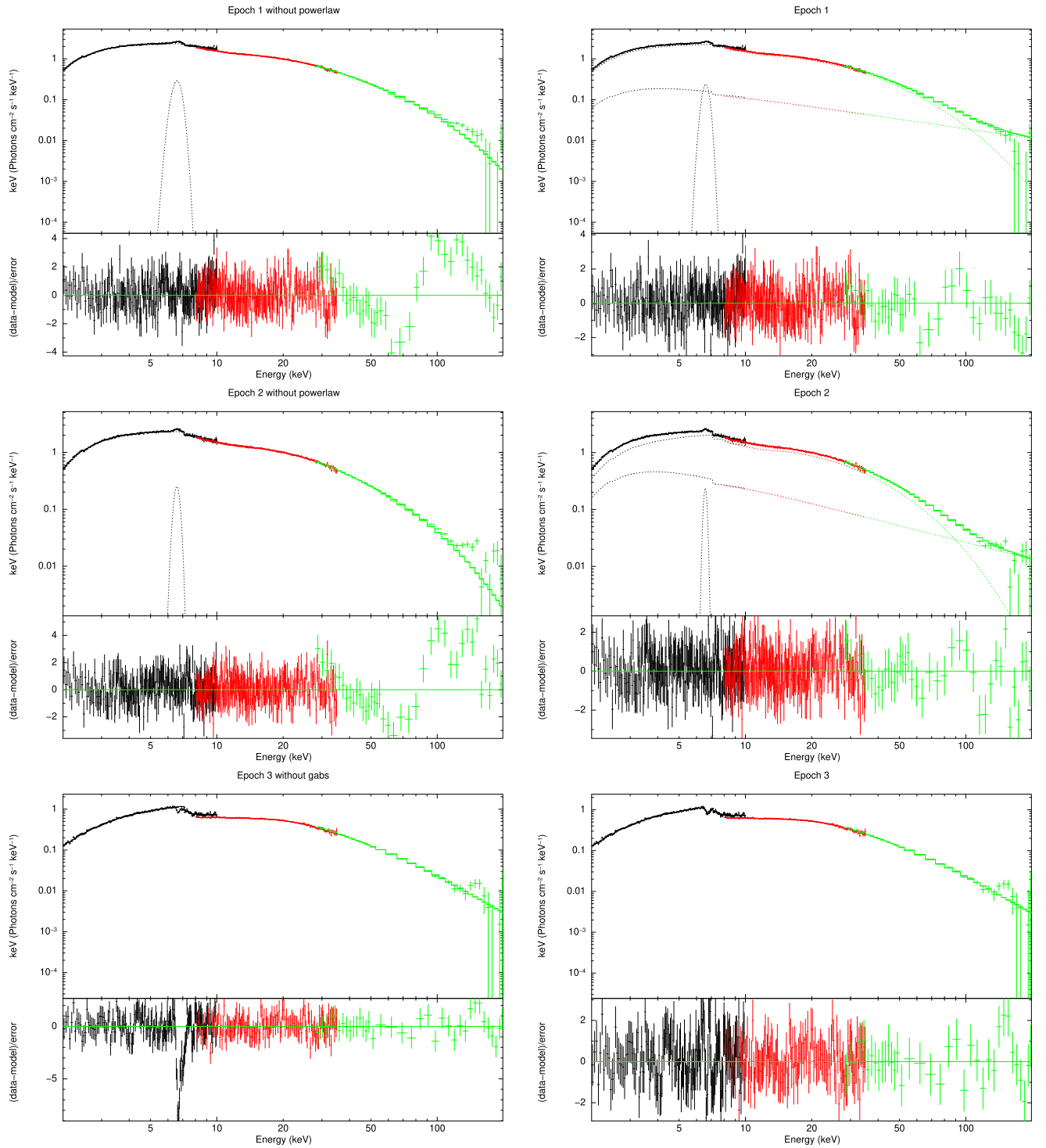
**Figure 3.** The panels show different epochs during the flare. The LE, ME, and HE are noted as follows: 2–10, 10–35, and 27–200 keV, respectively. The parameters and other details of the fittings are listed in Table 1. For the bottom right panel, we find that the *powerlaw* component is not required.

iron abundance of the material decrease, but the reflection fraction increases. In epoch 3, the column density is about a factor of a few larger than that in epochs 1 and 2. These results may be understood in a scenario of jet/wind transitions where the disk magnetic field plays an important role (see Figure 5).

Although the origin of the observed huge flare in GRS 1915 +105 is still largely unclear, it can, in principle, be driven by either the viscous instabilities in the accretion disk or the magnetic field. The former is most likely relevant to the canonical relation

of the wind/jet to the spectral states. The activity observed in the radio band at a time around the X-ray flares may imply that at least part of the flare can be related to the jet ejection (Koljonen et al. 2019; Murata et al. 2019; Trushkin et al. 2019a, 2019b, 2020).

In our results shown in Figure 3, the significant residuals in epochs 1 and 2 above 50 keV can be regarded as a "hard tail" with a power-law index of ∼2, which may be associated with a relativistic jet formed with a large-scale collimated magnetic
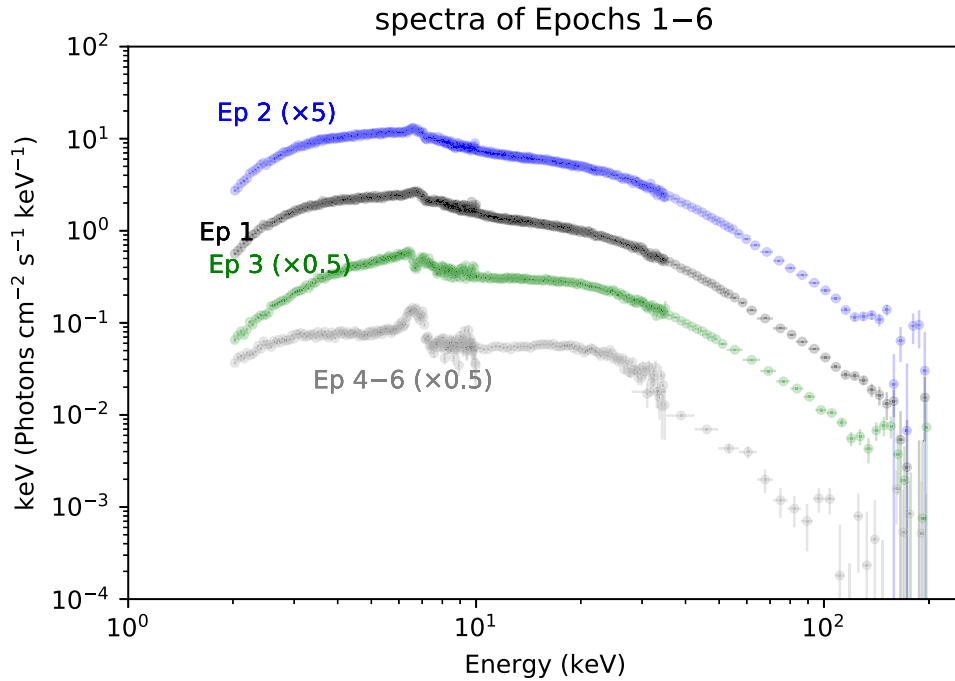
**Figure 4.** The picture shows the spectra of six epochs of the huge flare. For epochs 4–6, we combine the spectra for higher significance. The colors of the points follow Figure 1. Epochs 1–6 show significant evolution.

field near the BH (Reig & Kylafis 2016). Meanwhile, the radio activities and flares that occurred around the X-ray flares also suggest the correlation of the X-ray flare with the relativistic jet (Mirabel & Rodríguez 1994; Trushkin et al. 2020). On the other hand, such a hard tail weakens when the flare luminosity becomes lower in epoch 3, and, instead of having a Gaussian emission line in epochs 1 and 2, an absorption line shows up at $\sim$6.78 keV. We would like to note that the limited energy resolution of LE does not allow us to constrain the velocity of the wind; hence, the possible presence of a "failed" disk wind with low velocity cannot be ruled out. Nevertheless, such a wind feature, as discussed in Miller et al. (2020), is most likely driven by a magnetic field.

Theoretically, the formation of large-scale magnetic fields near a BH is usually believed to highly relate to the advection of the accretion flow, such as the accretion disk and corona. The large-scale magnetic field can be efficiently dragged inward by the corona above the disk, the so-called "coronal mechanism" (Beckwith et al. 2009), which provides a way to solve the difficulty of field advection in a geometrically thin accretion disk. But the maximum power of the jet accelerated by the magnetic field advected by the corona is less than 0.05 Eddington luminosity (Cao 2018). Li & Cao (2019) suggested that the external field can be efficiently dragged inward in a thin disk with magnetic outflows to form the large-scale magnetic field that plays a main role in acceleration and collimation of the jet. Consequently, the disk structure will be altered in the presence of outflows, especially for strong outflows, which can carry both mass and angular momentum from the disk. Based on their model, the disk may work as a bridge to connect the jet and wind during the flare in case a magnetic field is at work. Our results show different disk properties in its inner radius according to the switch off/on of the jet and disk wind during the flare, although the disk emissions are probably too weak to be detected directly.

A jet is usually observed in the absence of a disk wind. By revealing a surprisingly simple jet-quenching mechanism in GRS 1915+105, Neilsen & Lee (2009) pointed out fundamental new insights into the long-term disk–jet coupling around accreting BHs and left attractive evidence of the mechanism by which stellar-mass BHs can regulate their own growth. The disk wind in the soft X-ray states can be so powerful in carrying away so much mass that matter is halted from flowing into the jet. Our results from the flaring GRS 1915+105 show that wind presents at a flux lower than the jet during epoch 3. The absence of a power-law component and a significant increase in $N_H$ may imply that epoch 3 is intrinsically softer, rather than a typical hard state. The detection of the transition between the jet and wind can be broadly consistent with Ponti et al. (2012). Using an ionization parameter $\log \xi \sim 2.5$–4, an electron density $n_e \sim 10^{14}$ cm$^{-3}$ from Neilsen et al. (2020), and a luminosity $L = L_{2\text{–}200} \sim 3.8 \times 10^{38}$ erg s$^{-1}$ during epoch 3, a launch radius of the wind can be estimated as $R_{\text{Launch}} = 1.96\text{–}10.96 \times 10^{10}$ cm according to the following formula (Tarter et al. 1969):

$$R_{\text{Launch}} = (L \times (n_e \xi)^{-1})^{1/2}. \tag{1}$$

Meanwhile, the Compton temperature $T_{\text{IC}}$ and Compton radius $R_{\text{C}}$ can be estimated as $0.67 \times 10^7$ K and $1.23 \times 10^{12}$ cm, respectively. Dubus et al. (2019) considered the contribution from radiation pressure at a luminosity close to Eddington (Proga & Kallman 2002; Done et al. 2018). Accordingly, the equations for $T_{\text{IC}}$ and $R_{\text{IC}}$ are shown as

$$\frac{T_{\text{IC}}}{10^7 \text{ K}} = \begin{cases} 4.2 - 4.6 \times \log(l/0.02) & \text{if } l < 0.02 \\ 0.36 \times (l/0.02)^{1/4} & \text{if } l \geqslant 0.02 \end{cases}, \tag{2}$$

$$R_{\text{IC}} \approx 10^{12} \times \frac{M}{10\,M_\odot} \times \frac{10^7 \text{ K}}{T_{\text{IC}}} \times \left(1 - \sqrt{2}\,\frac{L}{L_{\text{Edd}}}\right), \tag{3}$$
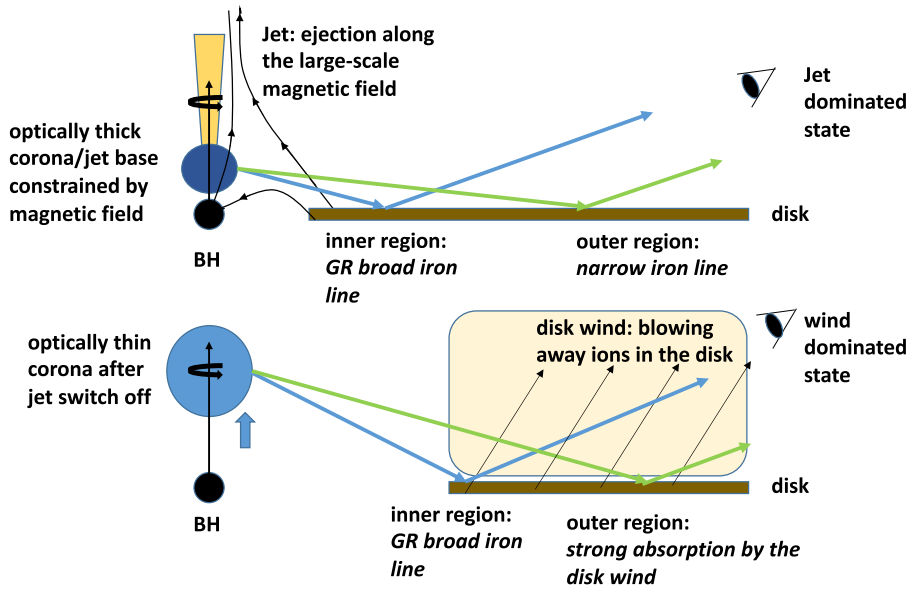
**Figure 5.** Simplified sketch of the two states during the huge flare. The top panel illustrates the jet-dominated state with a large-scale collimated magnetic field threading the accretion disk near $R_{\rm ISCO}$ and the matter ejected along the black arrow lines (field lines). The optically thick corona/jet base is constrained near the BH, which irradiates the inner and outer regions of the accretion disk, where the broad and narrow iron lines are produced, respectively. The bottom panel shows the circumstance during the wind-dominated state. The inner radius of the accretion disk moves outward, and the collimated magnetic field turns into a diverging field anchoring the outer region of the accretion disk. The corona expands to a larger scale and becomes optically thin after the jet switches off. The reflection component shows different properties because of the outflow absorption. The iron absorption line implies a magnetic field–driven wind or stable absorber on the disk.

where $l = L/L_{\rm Edd}$. Since the $R_{\rm Launch}$ is far less than $0.2R_{\rm IC}$, the absorption wind in epoch 3 is not likely to be thermally driven. This suggests that a large-scale magnetic field may be occasionally at work for boring both the jet and disk wind and responsible for their mutual transitions.

In this "unusual" low-luminosity state of GRS 1915+105, a relatively weaker flare was detected by NICER. The flare reported in this work has a longer duration and higher luminosity than the flare reported by NICER (Neilsen et al. 2019; Neilsen et al. 2020). Our spectral results in epoch 3 are roughly consistent with those derived at the peak of the NICER flare (Neilsen et al. 2019; Neilsen et al. 2020). We note that the source flux in epoch 3 turns out to be comparable to that of the peak flux in the NICER flare. Miller et al. (2020) investigated the highly obscured state in the "unusual" low-luminosity period and ended up with a "failed wind." They argued that the wind could not achieve the local escape velocity and thus led to a heavily obscured local environment. It seems that the canonically prohibited disk wind in the hard state can be born with an immaturity, known as a "failed wind," in the presence of the magnetic field. Thus, a "successful" disk wind could be the consequence of having a stronger magnetic field, which may be the case as observed in the huge flare of GRS 1915+105.

In summary, we speculate that the scenario illustrated in Figure 5 may account for the spectral evolution as observed in the flare decay from epochs 1 and 2 to epoch 3. In epochs 1 and 2 (top panel of Figure 5), a jet is formed from channeling the accretion material from the disk via a large-scale magnetic field. The emissions from the jet base are reflected at the different parts of the disk, where at the inner part, a broadened Fe line is formed, and at the outer part, the regular Fe emission lines are produced. Once the flare enters epoch 3, as shown in the bottom panel of Figure 5, the inner disk recedes from the central BH, and the large-scale magnetic field that connects the former jet and disk accretion material breaks. Further investigation of the reflection component in spectral fitting with *relxilllp* shows that

the height of the central illuminating source can largely increase in epoch 3 (see Table 1). Also, a similar trend of having a receding disk in epoch 3 is present with *relxilllp*. The height of the corona can increase significantly from $\sim 6\,R_{\rm g}$ during epochs 1 and 2 to $\sim 30\,R_{\rm g}$ during epoch 3. Although the errors of $R_{\rm in}$ are relatively large, an overall trend of having a receding inner disk is also visible with *relxillp*.

The constraint upon the geometry of the illuminating source may be responsible for the difference of the two reflection models in the measurement of the disk radius. In both models, the power-law component shows up in epochs 1 and 2 but disappears in epoch 3. This gives evidence of the jet evolving fainter in epoch 3. Also, the larger height of the illuminating source in epoch 3 may suggest that either a higher corona or a faint jet merges into the corona, which results in a larger emission region (see Figure 5). The open field lines accelerate and channel part of the accretion materials into the disk wind, part of which is the ionized Fe. The interception of the central light source by such a disk wind can result in an Fe absorption line and additional absorption with fairly large coverage. In epoch 3, the larger spectral index and higher cutoff energy of the central light house may suggest that the collapsed jet is merged into the corona and hence forms a central hot region with a relatively larger height but smaller optical depth with respect to those in epochs 1 and 2. Consequently, we observe a larger reflection fraction. As for the drop in the Fe abundance and emission line, it is probably due to the absorption by the disk wind, which may lead to a decrement of Fe line production at the outer disk.
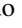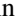
## 5. Conclusions

In this study, we have analyzed the largest X-ray flare of the microquasar GRS 1915+105 recorded in the Insight-HXMT data set during its "unusual" low-luminosity state. The joint diagnostics of this flare with Insight-HXMT in a rather broad energy band and the context of contemporary observations in

other wavelengths reveals a peculiar flaring source behavior, which may suggest that the BH X-ray binary activity may occasionally be under the control of the presence of a large-scale magnetic field and end up with behavior different from the canonical ones.

### ORCID iDs

L. D. Kong ⓘ https://orcid.org/0000-0003-3188-9079
S. N. Zhang ⓘ https://orcid.org/0000-0001-5586-1017
L. Tao ⓘ https://orcid.org/0000-0002-2705-4338
M. Y. Ge ⓘ https://orcid.org/0000-0002-2749-6638
F. J. Lu ⓘ https://orcid.org/0000-0003-3248-6087
J. L. Qu ⓘ https://orcid.org/0000-0002-9796-2585
Y. Chen ⓘ https://orcid.org/0000-0001-9834-2196
Q. C. Bu ⓘ https://orcid.org/0000-0001-5238-3988
H. Gao ⓘ https://orcid.org/0000-0002-3100-6558
S. M. Jia ⓘ https://orcid.org/0000-0002-5203-8321
B. Li ⓘ https://orcid.org/0000-0002-0238-834X
C. K. Li ⓘ https://orcid.org/0000-0001-5798-4491
G. Li ⓘ https://orcid.org/0000-0001-5067-1599
X. F. Li ⓘ https://orcid.org/0000-0002-2793-9857
B. S. Liu ⓘ https://orcid.org/0000-0002-5853-9290
Q. Luo ⓘ https://orcid.org/0000-0003-1853-7810
Y. L. Tuo ⓘ https://orcid.org/0000-0003-3127-0110
Q. Q. Yin ⓘ https://orcid.org/0000-0001-7580-1513

### References

Aoki, M., Negoro, H., Kobayashi, K., et al. 2020, ATel, 13652, 1
Arnaud, K. A. 1996, in ASP Conf. Ser. 101, Astronomical Data Analysis Software and Systems V, ed. G. H. Jacoby & J. Barnes (San Francisco, CA: ASP), 17
Beckwith, K., Hawley, J. F., & Krolik, J. H. 2009, ApJ, 707, 428
Belloni, T., Klein-Wolt, M., Méndez, M., van der Klis, M., & van Paradijs, J. 2000, A&A, 355, 271
Cao, X. 2018, MNRAS, 473, 4268
Cao, X., Jiang, W., Meng, B., et al. 2020, SCPMA, 63, 249504
Castro-Tirado, A. J., Brandt, S., & Lund, N. 1992, IAUC, 5590, 2
Chen, Y., Cui, W., Li, W., et al. 2020, SCPMA, 63, 249505
Dauser, T., Garcia, J., Parker, M. L., Fabian, A. C., & Wilms, J. 2014, MNRAS, 444, L100
Done, C., Tomaru, R., & Takahashi, T. 2018, MNRAS, 473, 838
Dubus, G., Done, C., Tetarenko, B. E., & Hameury, J.-M. 2019, A&A, 632, A40
García, J., Dauser, T., Lohfink, A., et al. 2014, ApJ, 782, 76
Greiner, J., Cuby, J. G., McCaughrean, M. J., Castro-Tirado, A. J., & Mennickent, R. E. 2001, A&A, 373, L37
Guo, C.-C., Liao, J.-Y., Zhang, S., et al. 2020, arXiv:2003.06260
Homan, J., Neilsen, J., Allen, J. L., et al. 2016, ApJL, 830, L5
Homan, J., Neilsen, J., Gendreau, K., et al. 2019, ATel, 13308, 1
Iwakiri, W., Negoro, H., Nakajima, M., et al. 2019, ATel, 12761, 1
Jithesh, V., Maqbool, B., Dewangan, G. C., & Misra, R. 2019, ATel, 12805, 1
Klein-Wolt, M., Fender, R. P., Pooley, G. G., et al. 2002, MNRAS, 331, 745
Koljonen, K., Vera, R., Lahteenmaki, A., & Tornikoski, M. 2019, ATel, 12839, 1
Koljonen, K. I. I., & Tomsick, J. A. 2020, A&A, 639, A13
Li, J., & Cao, X. 2019, ApJ, 872, 149
Liao, J.-Y., Zhang, S., Chen, Y., et al. 2020a, arXiv:2004.01432
Liao, J.-Y., Zhang, S., Lu, X.-F., et al. 2020b, arXiv:2005.01661
Liu, C., Zhang, Y., Li, X., et al. 2020, SCPMA, 63, 249503
Miller, J. M., Zoghbi, A., Raymond, J., et al. 2020, arXiv:2007.07005
Mirabel, I. F., & Rodríguez, L. F. 1994, Natur, 371, 46
Murata, K. L., Kawai, N., Yamagishi, M., et al. 2019, ATel, 12769, 1
Neilsen, J., Homan, J., Gendreau, K., et al. 2019, ATel, 12793, 1
Neilsen, J., Homan, J., Steiner, J. F., et al. 2020, ApJ, 902, 152
Neilsen, J., & Lee, J. C. 2009, Natur, 458, 481
Neilsen, J., Remillard, R. A., & Lee, J. C. 2011, ApJ, 737, 69
Ponti, G., Fender, R. P., Begelman, M. C., et al. 2012, MNRAS, 422, L11
Proga, D., & Kallman, T. R. 2002, ApJ, 565, 455
Reid, M. J., McClintock, J. E., Steiner, J. F., et al. 2014, ApJ, 796, 2
Reig, P., & Kylafis, N. 2016, A&A, 591, A24
Remillard, R. A., & McClintock, J. E. 2006, ARA&A, 44, 49
Svinkin, D., Golenetskii, S., Aptekar, R., et al. 2019, ATel, 12818, 1
Takagi, R., Kobayashi, K., Negoro, H., et al. 2020, ATel, 13478, 1
Tarter, C. B., Tucker, W. H., & Salpeter, E. E. 1969, ApJ, 156, 943
Trushkin, S. A., Nizhelskij, N. A., Tsybulev, P. G., Bursov, N. N., & Shevchenko, A. V. 2019a, ATel, 12855, 1
Trushkin, S. A., Nizhelskij, N. A., Tsybulev, P. G., Bursov, N. N., & Shevchenko, A. V. 2019b, ATel, 13304, 1
Trushkin, S. A., Nizhelskij, N. A., Tsybulev, P. G., Bursov, N. N., & Shevchenko, A. V. 2020, ATel, 13442, 1
Vishal, J., & Banerjee, D. P. K. 2019, ATel, 12806, 1
Wilms, J., Allen, A., & McCray, R. 2000, ApJ, 542, 914
Zhang, S., Lu, F. J., Zhang, S. N., & Li, T. P. 2014, Proc. SPIE, 9144, 914421
Zhang, S.-N., Li, T., Lu, F., et al. 2020, SCPMA, 63, 249502
Zoghbi, A., Miller, J. M., King, A. L., et al. 2016, ApJ, 833, 165